Electronic Supplementary Information (ESI)

Self-templating 2D supramolecular networks: A new avenue to reach control over a bilayer formation

A. Ciesielski, A. Cadeddu, C.-A. Palma, A. Gorczyński, V. Patroniak, M. Cecchini* and P. Samorì*

E-mail: samori@unistra.fr, mcecchini@unistra.fr

Table of Contents

1. Experimental Procedures:

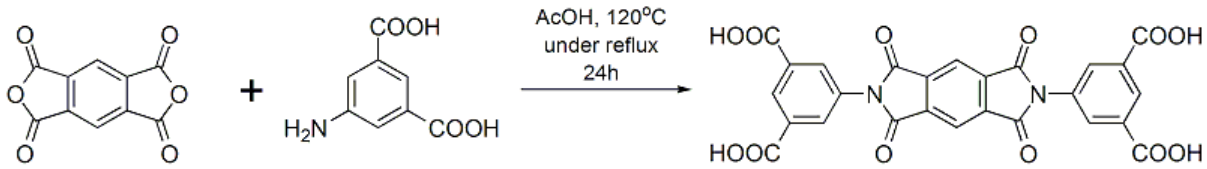

Figure S1. Scheme presenting the synthesis of 5,5'-(1,3,5,7-tetraoxopyrrolo[3,4-f]isoindole-2,6-diyl)diisophthalic acid (**1**).

*Synthesis of 5,5'-(1,3,5,7-tetraoxopyrrolo[3,4-f]isoindole-2,6-diyl)diisophthalic acid (**1**)*: Benzene-1,2,4,5-tetracarboxylic dianhydrate (3.2g, 14.67 mmol) and 5-aminoisophthalic acid (5.32g, 29.34 mmol) were placed in a round bottom flask and 30 ml of glacial acetic acid was added. The mixture was stirred and heated at 120°C for 24 hours under reflux. To the obtained white precipitate, distilled water and $CHCl_3$ were added. After drying, precipitate was found to change the color from white to yellowish. Additional purification did not appear to be of significant importance. Yield: 7.2g (13.22 mmol, 91%). ^{1}H NMR (400 MHz, [D6]DMSO): δ = 8.55 (t, J = 1.57 Hz, 2H), 8.45 (s, 2H), 8.38 (d, J = 1.57 Hz, 4H). ^{13}C NMR (400 MHz, [D6]DMSO): δ = 166.34, 165.67, 137.63, 132.88, 132.59, 132.35, 129.87, 118.46. Fast atom bombardment - mass spectrometry (FAB-MS): *m/z* = 545.3 $[M+H]^+$. Microanalysis: calcd (%) for $C_{26}H_{12}N_2O_{12}$: C 57.36, H 2.22, N 5.15, O 35.27; found C 57.22, H 2.12, N 5.23, O 35.43.

^{1}H NMR spectra were recorded using a Bruker Avance 400 spectrometer at 400 MHz. Chemical shifts are given in ppm. The residual solvent peak was used as reference for calibration ($CDCl_3$: 7.26 ppm, $[D_6]$DMSO: 2.50 ppm). ^{13}C NMR spectra were recorded using a Bruker Advance 400 spectrometer at 100 MHz. All spectra were measured in broadband decoupled conditions. Chemical shifts are given in ppm. The residual solvent peak were taken as reference ($CDCl_3$: 77.0 ppm, $[D_6]$DMSO: 39.43). Unless otherwise noted, spectra were recorded at 25°C. Elemental analyses were performed on a home built apparatus of the "Service d'Analyses du CNRS" (Lyon) and at the Service de Microanalyse, Université de Strasbourg. Data are given in percentage. Fast atom bombardment (FAB) mass spectra were recorded with a ZAB-HF VG spectrometer with m-nitrobenzyl alcohol as the matrix.

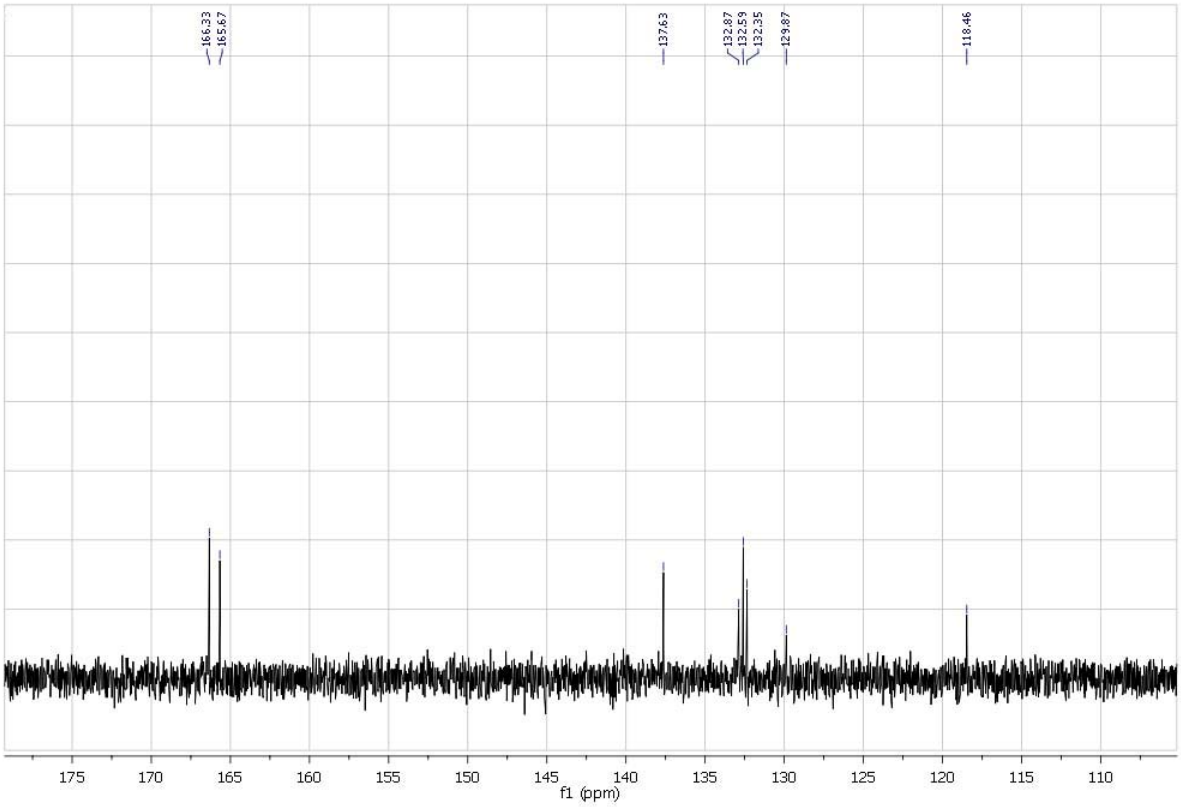

Figure S2. ^{13}C NMR spectrum of **1** ([D_6]DMSO, 400 MHz).

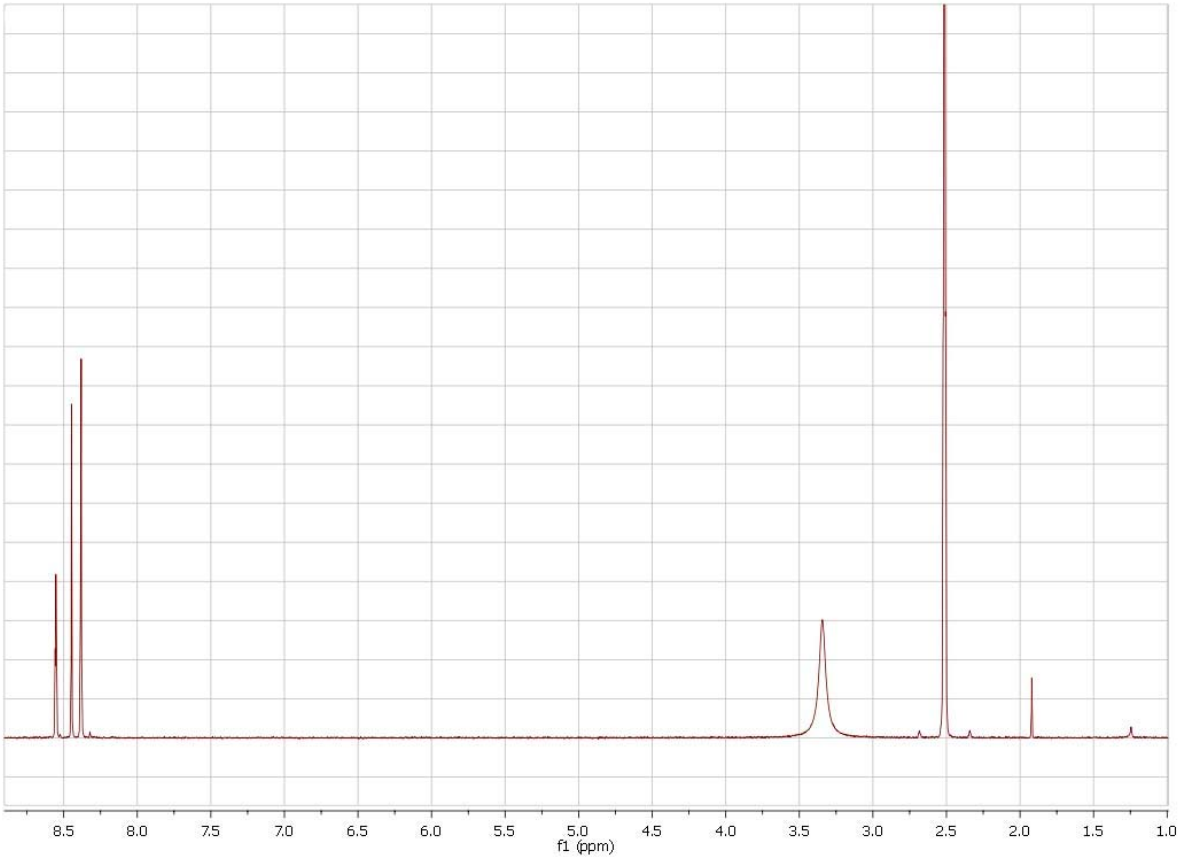

Figure S3. ^{1}H NMR spectrum of **1** ([D_6]DMSO, 400 MHz).

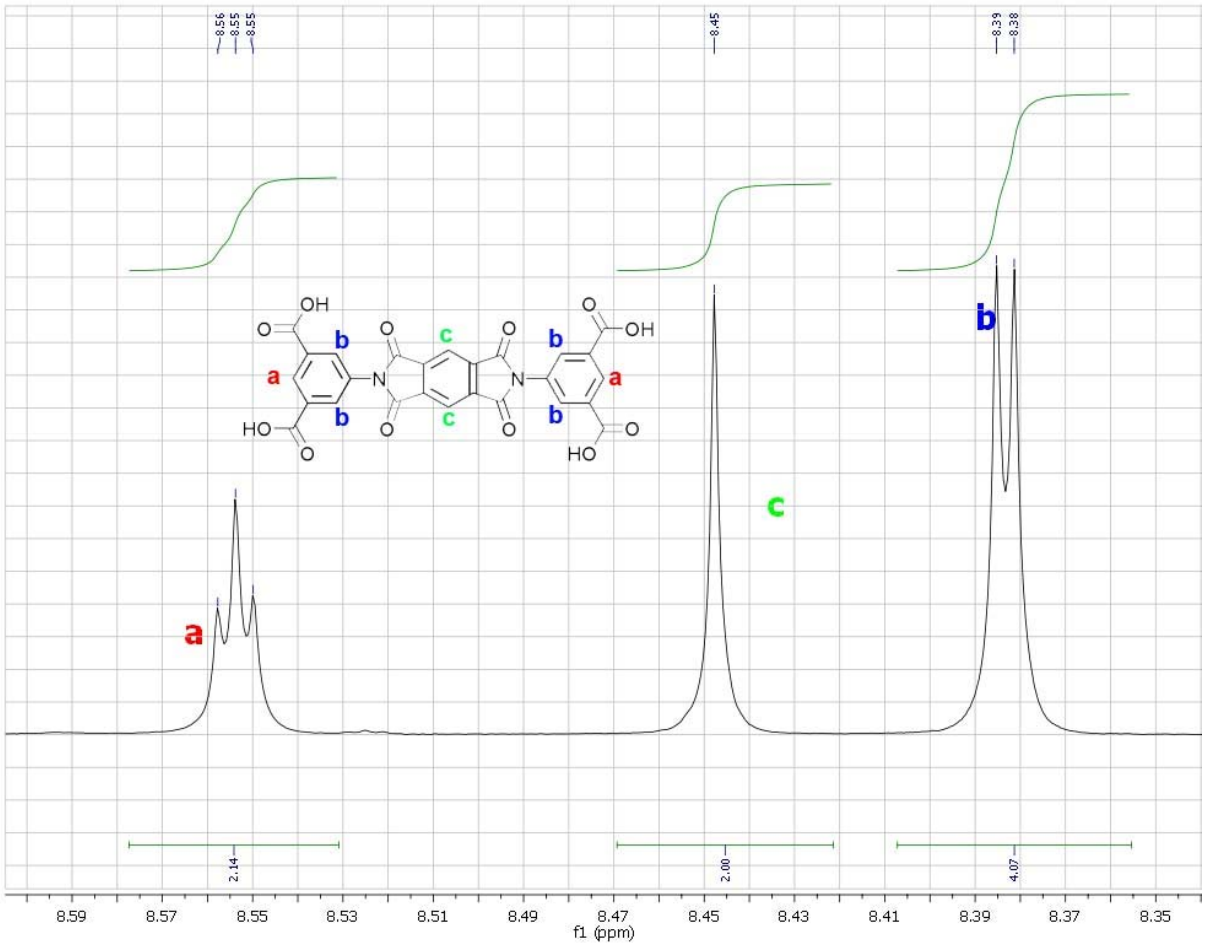

Figure S4. Proposed pick assignment of **1** on the ^{1}H NMR spectra recorded at 25^{o}C.

2. Self-assembly of C_2-symmetric tetracarboxylic acid (TCA) derivatives.

C_2-symmetric tetracarboxylic building blocks self-assemble through the formation of H-bonds in either *p2* symmetry 2D "brick-wall" architectures (Fig.S5a), so-called "close-packed" architectures (Fig.S5b) or *p6* symmetry 2D Kagomé networks (Fig.S5c), depending on the size of the core.[1] Some of the TCA derivatives can self-assemble randomly on substrate surface, leading to the formation of organic glass structures.[2]

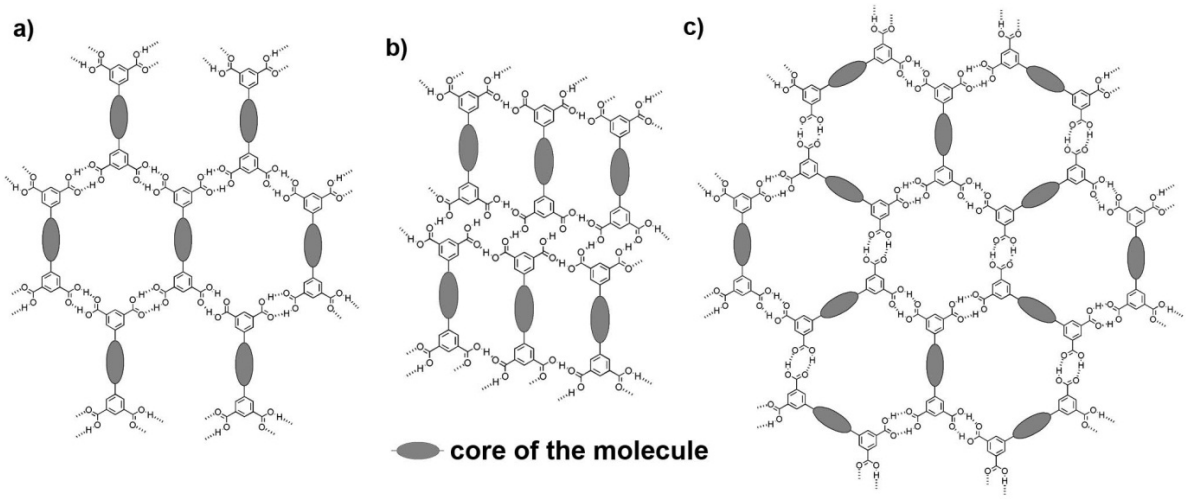

Figure S5. a) brick-wall, b) close-paced, and c) Kagomé architectures formed by tetracarboxylic derivatives.

3. STM investigation

Scanning Tunneling Microscopy (STM) measurements were performed using a Veeco scanning tunneling microscope (multimode Nanoscope III, Veeco) at the interface between highly oriented pyrolitic graphite (HOPG) and a supernatant solution, by using a scanner A (Veeco), therefore by mapping an area of 1µm × 1µm. Diluted solutions of **1** were applied to the basal plane of the surface. For STM measurements the substrates were glued on a magnetic disk and an electric contact is made with silver paint (Aldrich Chemicals). The STM tips were mechanically cut from a Pt/Ir wire (90/10, diameter 0.25 mm). The raw STM data were processed through the application of background flattening and the drift was corrected using the underlying graphite lattice as a reference. The latter lattice was visualized by lowering the bias voltage to 20 mV and raising the current to 65 pA. Mother solution of 5,5'-(1,3,5,7-tetraoxopyrrolo[3,4-f]isoindole-2,6-diyl)diisophthalic acid (**1**) was dissolved in DMSO at 95ºC and diluted with 1-heptanoic acid to give, 280 µM, 28 µM and 2.8 µM solutions. It is important to note that molecule **1** was visualized at the HOPG–solution interface only upon using 1-heptanoic acid as solvent. Study of this system in different solvents, 1-phenyloctane, 1,2,4-trichlorobenzene and tetradecane, did not produced any ordered monolayers. For this reason, we continued our study using 1-heptanoic as a solvent.

STM imaging was carried out in constant height mode yet without turning off the feedback loop, to avoid tip crashes. Under such conditions, the distance tip-surface during scanning is not kept constant, despite the tunneling current is the signal that is sampled and shown in Figs. 1 and 2 in the main text. In practice it is the “feedback image” and not a “constant

height" image the real output, which tries to follow an *iso*-current countour. The "constant height" image is in fact the feedback complementary image, and should called, the "current error" image. When the current error image tends to zero the feedback image is a true "constant current" image, i.e. the *piezo* reacts immediately to the changes of current to follow an *iso*-current path, so that we follow exactly the contour of one electronic state or orbital, allowing the imaging of molecular orbitals. Monolayer pattern formation was achieved by applying onto freshly cleaved HOPG a 4μL of a solution that was heated at warm 60-70ºC to improve the solubility. Self-assembled monolayers were prepared by applying a 4μL drop of 280 μM, 28 μM and 2.8 μM solutions of **1**, thus containing 1.12×10^{-9}, 1.12×10^{-10}, 1.12×10^{-11} molecules respectively. Noteworthy, the amount of molecules needed to form tightly packed self-assembled monolayer of **1** on $1cm^2$ of HOPG surface (no voids present in the structure) is equal to 1.18×10^{-10} (area of van der Waals projection of molecule **1** on the surface was estimated as 1.44 nm^2).The STM images were recorded only after achieving a negligible thermal drift. By using lower temperature during the heating process, small precipitating agglomerates were observed. On the other hand, in-situ STM experiments at variable temperature cannot be performed using our set-up. Several additional experiments were performed using the solutions with concentrations of 140 μM, 70 μM in order to study the potential growth of adlayer structures of **1** on top of self-assembled 2D Kagomé structures. However, such a phenomenon was never observed. All of the molecular models were minimized with Chem3D at the MM2 level and processed with QuteMol visualization software.[3]

Figure S6 shows STM current images (viz. images recorded in current error mode) of the obtained physisorbed monolayer of **1** from 28 μM solution, featuring a polycrystalline Kagomé structure (***K1***).

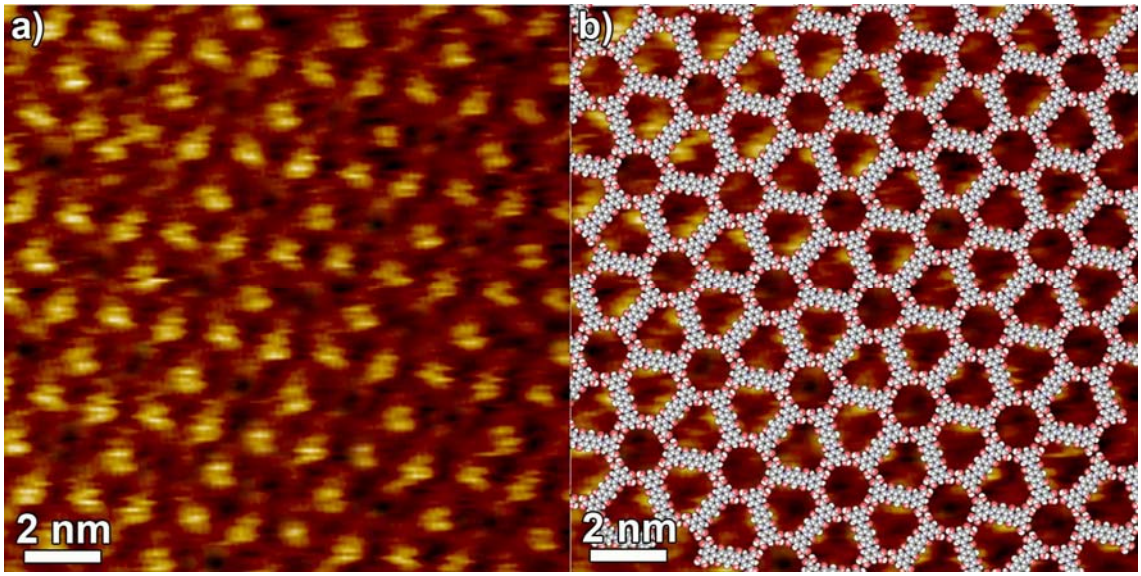

Figure S6. a,b) STM current images of a film of supramolecular H-bonded Kagomé structure at the liquid-graphite interface self-assembled from 28 μM solution of **1** in 1-heptanoic acid forming the 2D nanopattern. Tunneling parameters: Average tunneling current (I_t) = 25pA, tip bias voltage (V_t) = 400 mV. Unit cell parameters: a = (2.7 ± 0.2) nm, b = (2.8 ± 0.2) nm, α = (60 ± 2)°, leading to an area A = (6.5 ± 0.5) nm2, where each unit cell contains three molecules 1, thus the are occupied by single molecule 1 is equal to Amol = (2.17 ± 0.17) nm2.

Figure S7 shows STM current of the obtained physisorbed monolayer of **1** from 2.8 μM solution, featuring a polycrystalline brick-wall architecture, which consists of hundreds of square nanometers large crystalline domains.

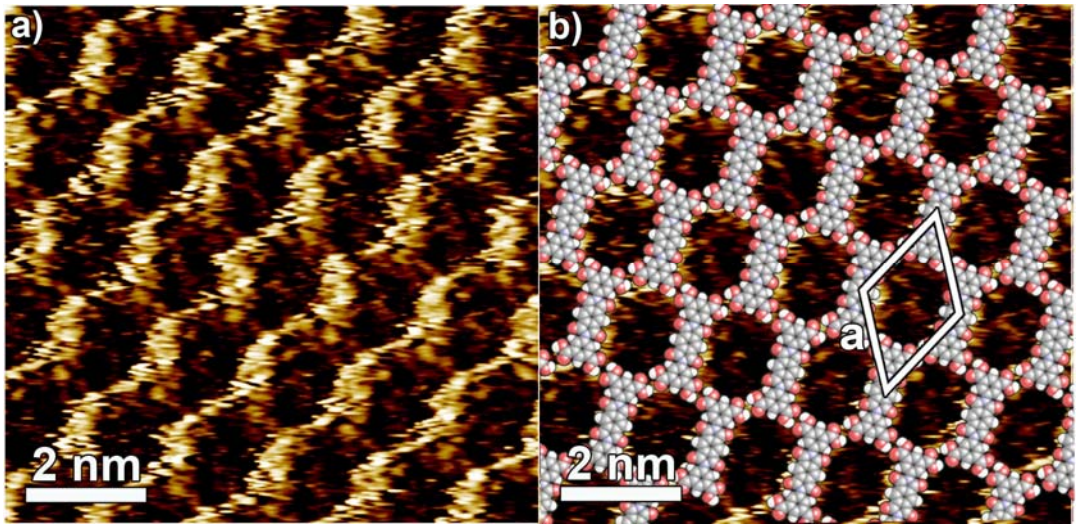

Figure S7. a,b) STM current images of a film of supramolecular H-bonded brick-wall structure at the liquid-graphite interface, self-assembled from 2.8 μM solution of **1** in 1-heptanoic acid forming the 2D nanopattern. Tunneling parameters: I_t = 25pA, V_t = 400 mV. Unit cell parameters: a = (1.9 ± 0.2) nm, α = (57 ± 2)°, leading to an area A = (3.0 ± 0.4) nm2, where each unit cell contains one molecule 1.

Figure S8 shows the series of the STM current images of the obtained physisorbed monolayer of **1** after re-adsorption of molecules. Interestingly observed monolayer slightly differs from the one obtained from 28 µM solution of **1** (Fig. S6a). As indicated in Fig. S8a appearance of additional spots (marked in red) was observed; whereas distribution of spots marked in white perfectly correspond to the ***K1*** monolayer.

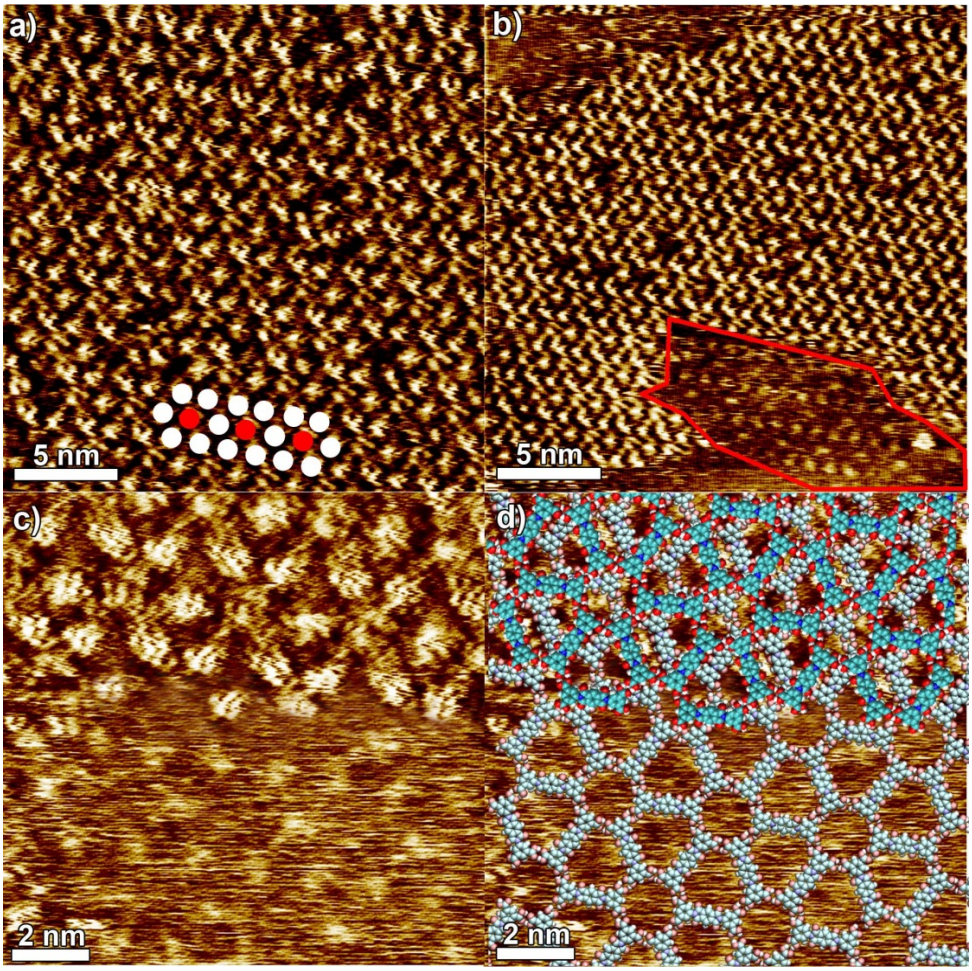

Figure S8. a-c) Series of STM current images of a bilayer supramolecular H-bonded Kagomé structure at the liquid-graphite interface, self-assembled from 2.8 µM solution in 1-heptanoic. Tunneling parameters: Average tunneling current I_t = 25pA, V_t = 100 mV. d) Proposed molecular packing motif of bilayer structure of ***K1***.

Films prepared by using highly concentrated solutions, i.e. 280 µM revealed the formation of bilayer structures of ***K1*** (Fig. S9). By using such a high concentration we were not able to visualize domain boundaries, which would allow us to observe both monolayer and bilayer structures of ***K1*** as it was possible by investigating films prepared from 2.8 µM solutions. Observed supramolecular architectures are rather uniform, however several defects in the structure can be observe. Two types of defects were found on the large scale STM image: i) lower current intensity can be assigned to the missing molecules in the first layer

(marked with green arrows), since current intensity of the molecules form the top layer should be much higher than the molecules from the bottom layer; ii) areas unoccupied by molecules (marked with blue arrow).

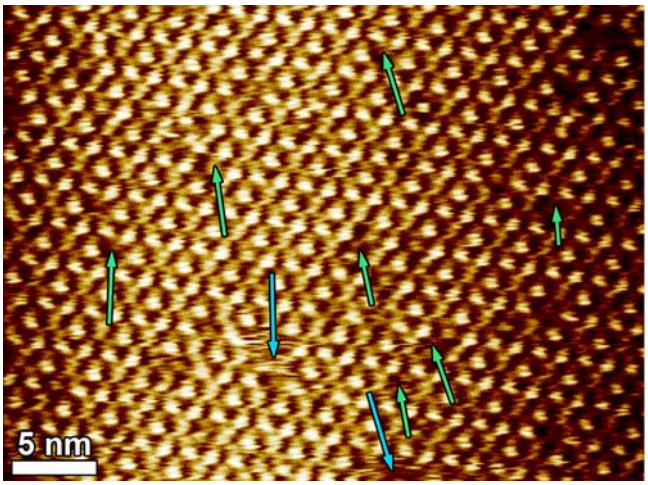

Figure S9. STM height image of a bilayer supramolecular H-bonded Kagomé structure at the liquid-graphite interface, self-assembled from 280 μM solution in 1-heptanoic. Tunneling parameters: I_t = 25pA, V_t = 100 mV.

4. Density functional theory (DFT)

The molecular geometries and molecular orbitals of **1** have been computed by using time-dependent density functional theory (TD-DFT).[4] Becke three-parameter hybrid exchange functional combined with the Lee–Yang–Parr correlation functional (B3LYP)[5] was used with the 6-31G++(d,p) basis set for geometry optimization. Gaussian 03[6] program, running on an SGI Altix 350 Linux server in 1 Itanium 2 processor at 1.5 GHz was used for calculations.[7] HOMO and LUMO orbitals and their energies have been estimated as -7.74 eV and -4.25 eV respectively.

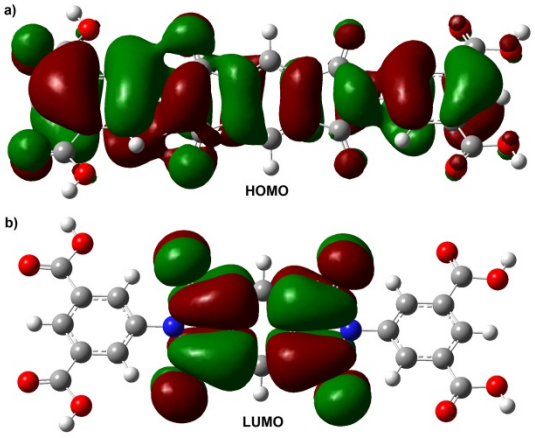

Figure S10. a) HOMO (highest occupied molecular orbital) and b) LUMO (lowest unoccupied molecular orbital) orbitals of **1** calculated by using TD-DFT.

When the substrate (being HOPG with a work function of ~4.7 eV or gold with a work function of ~5.1 eV[8] is positively biased, electrons from the Platinum/Iridium (Pt/Ir) tip (having a work function ~ 5.7 eV[9]) will flow to the sample assisted by the orbital aligned between the electrodes, which is normally the Lowest Unoccupied Molecular Orbital (LUMO) of an acceptor molecule. Figure S11 shows proposed packing motifs of both Kagomé and brick-wall assemblies, reconstructed by using LUMO orbitals representations computed by TD-DFT.

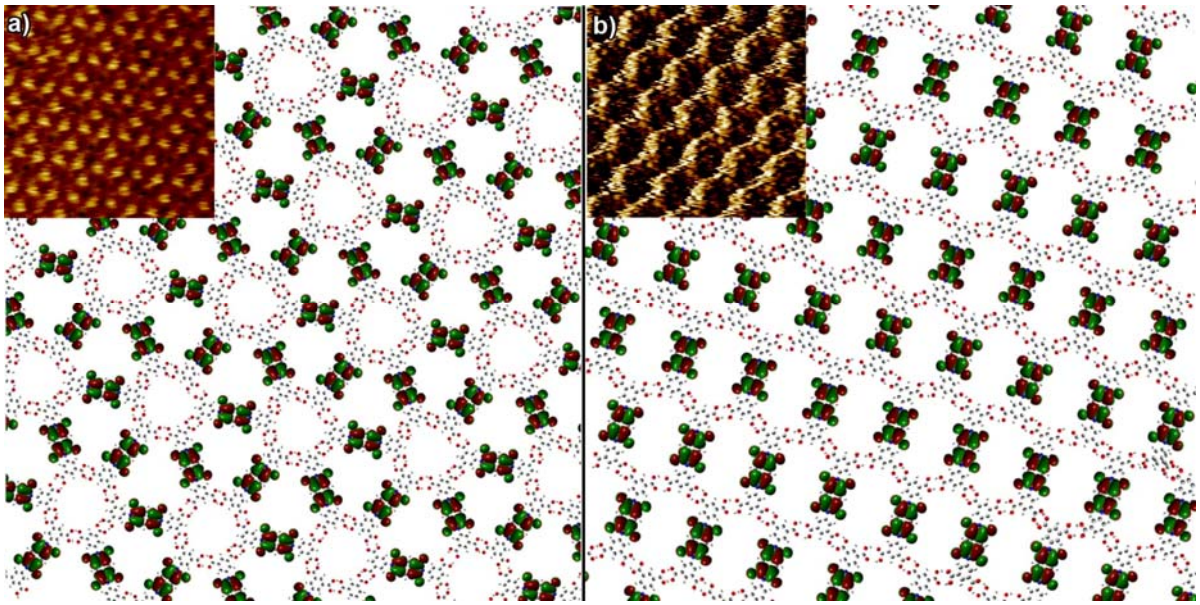

Figure S11. a) Kagomé and b) brick-wall assemblies of **1,** represented by LUMO orbitals.

5. Molecular Dynamics

In order to rationalize the formation of bilayer architectures of **1**, and what is even more important why the adlayer structures shows displacement with respect to the underlying monolayers, several all force-field calculations were performed with the program CHARMM[10] using the implementation in the c35b1 update. Parameterization of all investigated molecules was done through the Merck molecular force field MMFF94,[11] automatic module implemented in CHARMM.

Molecular models presented in this section as well as in Fig. 3 in the Main Text were processed with VMD visualization software.[12]

5.1 Kagomé on graphene

A 4480 graphene C-atom slab was embedded in a orthorhombic box of lengths equal to 98.38 and 119.14 Å with periodic boundary conditions (PBCs) to simulate an infinite graphene slab for all molecular force-field calculations. A distance cutoff of the size of the box side was applied to compute the non-bonded interactions. Molecular geometries were optimized by energy minimization in the presence of the graphene slab. In MMFF, all sp2 carbons were assigned the atom type 37 (aromatic), whereas graphene atoms (G) were assigned the atom type 2 (vinylic). The graphene slab was assigned 0 charges, and their coordinates were fixed in space by using CONS FIX. The results obtained by using those parameters, were found to be in good agreement with DFT calculations of the adsorption of neutral (poly)-aromatic and more generally π-conjugated systems on graphene.[13]

CHARMM Keywords:

```
SCALAR CHARGE SET 0 SELECT ATOM G* * * END
…
CONS FIX SELE SEGID G* END
…
CRYSTAL DEFINE ORTHO 98.38 119.14 100 90 90 90
CRYSTAL BUILD CUTOFF 90.0 NOPERATIONS 0
```

As a first step towards the understanding the formation of bilayer structure of ***K1***, we simulated the self-assembly of twelve-molecule-based Kagomé structure of **1** (***K1*$_{12}$**) on graphene slab. Five independent runs were done at 300, 400, 500, 600 and 700K for 100 ns in vacuum with periodic boundary conditions. The SHAKE[14] algorithm was used to fix the length of all covalent bonds, thus allowing for an integration time step of one femtosecond. Initially pre-assembled ***K1*$_{12}$** structure was placed 8Å above the graphene slab.

CHARMM Keywords:

```
SET NN 1
SET ID 1
SET NMOL 12
LABEL LABELNN
….
COOR TRANS XDIR 15.62 SELECT SEGID MMFF END
CALC ANGLE @NN*60
COOR ROTA ZDIR 1 PHI @ANGLE SELECT SEGID MMFF END
IF @ID .eq. 7 THEN
COOR TRANS XDIR -31.24 SELE SEGID MMFF END
ENDIF
IF @ID .eq. 8 THEN
COOR TRANS XDIR 31.24 SELE SEGID MMFF END
ENDIF
```

```
IF @ID .eq. 9 THEN
COOR TRANS YDIR -27.65 SELE SEGID MMFF END
COOR TRANS XDIR 15.62 SELE SEGID MMFF END
ENDIF
IF @ID .eq. 10 THEN
COOR TRANS XDIR 31.24 SELE SEGID MMFF END
ENDIF
IF @ID .eq. 11 THEN
COOR TRANS XDIR -31.24 SELE SEGID MMFF END
ENDIF
IF @ID .eq. 12 THEN
COOR TRANS YDIR 27.65 SELE SEGID MMFF END
COOR TRANS XDIR -15.62 SELE SEGID MMFF END
ENDIF
INCR ID
INCR NN
IF NN .le. @NMOL GOTO LABELNN
```

Pre-assembled ***K1$_{12}$*** structure have been optimized by applying 200 steps of Steepest Descent minimization (MINI SD), then the system was heated and equilibrated at desired temperature.

```
CHARMM Keywords:
SET TACT 300                                              !final temperature
SET HSTP 20000                                            !number of heating steps
DYNAMICS LEAP START -
     TIMESTP 0.002 NSTEP @HSTP -
     FIRSTT 100 FINALT @TACT TEMIC 10 IHTFRQ 1000         !system is heated by 10K
                                                          every 1000 steps
```

After achieving thermal equilibration, Langevin dynamics have been applied to model the dynamics of molecular systems.

```
CHARMM Keywords:
SET ESTP 10000000                                         !number of dynamic steps
…..
SCALAR FBETA SET 0.05          !sets the collision frequency of 0.05 per picosecond
```

K1$_{12}$ structures investigated at 300-600K shows no structural evolution, i.e. all H-bonds holding molecules **1** shows high stability during 100 ns of simulation time, only 2D translation and rotation of entire ***K1$_{12}$*** structures was observed. Figure S12 shows initial (Fig.S12a) and final (Fig.S12b) structures of ***K1$_{12}$*** architecture on graphene substrate investigated at 300K, which well represents the dynamics of Kagomé assemblies investigated in the 300-600K temperature range.

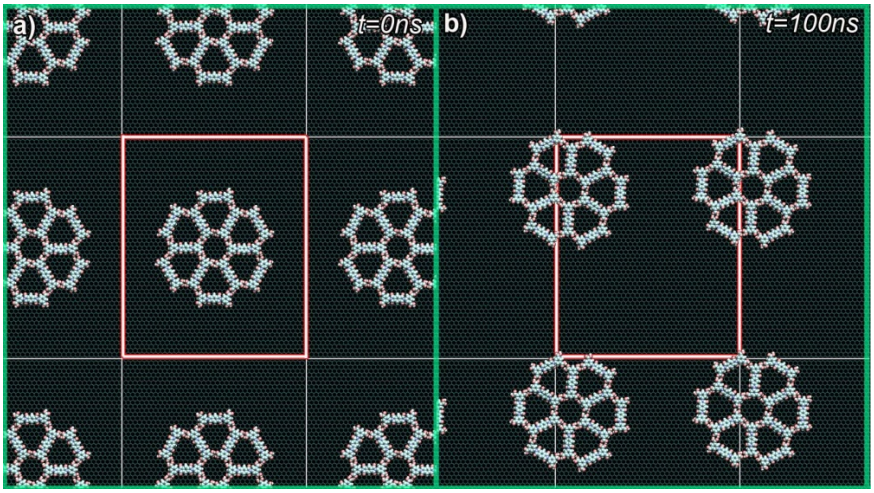

Figure S12. a) View of a manually pre-formed ***K1*$_{12}$** structure on top of graphene slab - initial structure, b) final structure of ***K1*$_{12}$** self-assembled structure investigated at 300K. Rectangular super-cells used for the calculations have been marked in red.

Interestingly, simulations of ***K1*$_{12}$** architecture on graphene at 700K, reveled large deformation of ***K1*$_{12}$** structure until rupture on the nanosecond timescale. Already after 10 ns of simulation, deformation of two H-bonds (indicated with white arrow on Fig. S13b) have been observed.

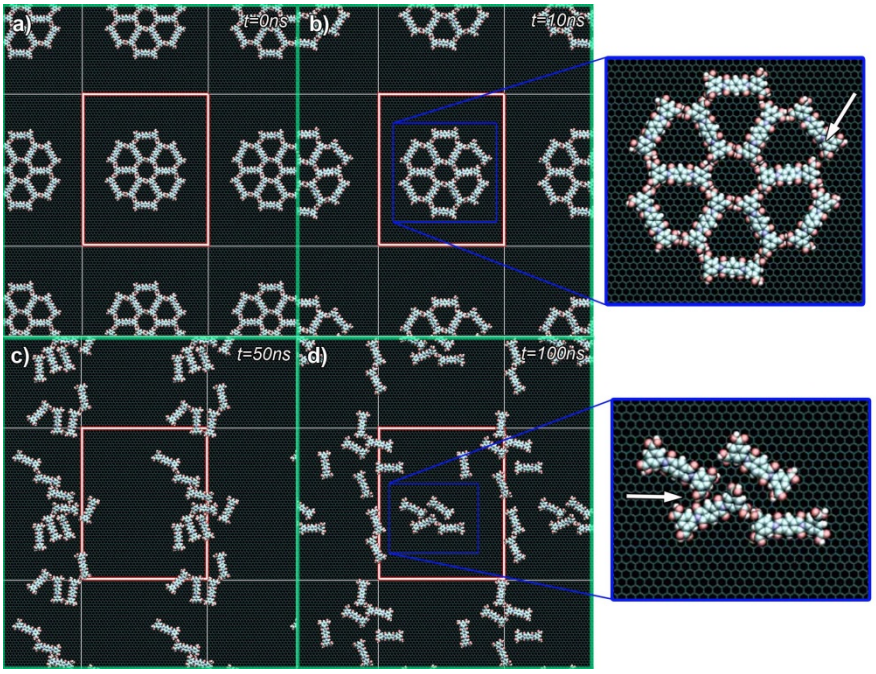

Figure S13. a-d) Representative visualization of ***K1*$_{12}$** self-assembled structure investigated at 700K. Rectangular super-cells used for the calculations have been marked in red.

Complete deformation of ***K1*$_{12}$** architecture and further formation of disordered architecture can be seen in Figure S13c. Such a glass-like architecture consists of brick-wall fragments as well as close-packed structures. Remarkably, self-assembled structures based on COOH···O=Core H-bonds have been detected, as shown in Figure S13d (indicated with white arrows), which indicates that oxygen atoms from the core of **1** can play an important role in the self-assembly processes.

In order to understand better the self-assembly process of **1**, especially the role of oxygen atoms from carbonyl groups in the formation of bilayer architectures, we decided to introduce two additional molecular building blocks (Fig.S14), in which the oxygen atoms from the core of the molecule have been replaced with =CH_2 groups (**2**) and sulfur atoms (**3**). It is important to note, that despite the change of the atomic charges, Pauling radius of carbonyl-oxygen atoms (1.4Å) has been replaced by larger substituence, i.e. 2.0Å in case of methylene group and 1.87Å when sulfur atoms were used. We also decided to compare those three molecules with the TCD derivative, which was reported (STM experiments) to form bilayer structures in the presence of templating C_{60} molecules (**4**).[1d]

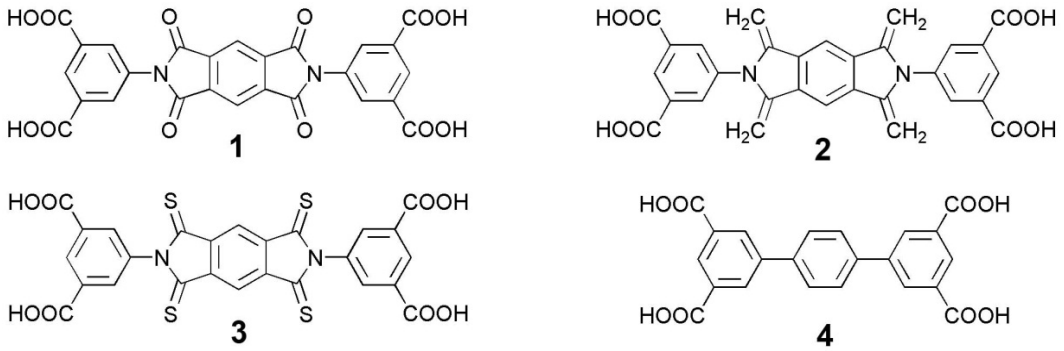

Figure S14. Chemical representation of investigated TCD derivatives **1**-**4**.

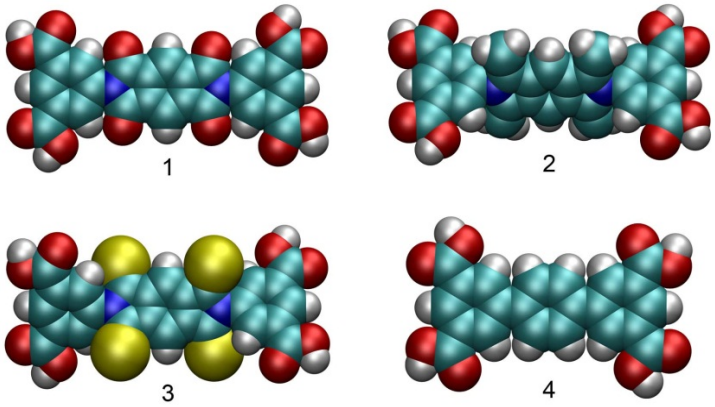

Figure S15. Minimized structures of investigated TCD derivatives **1**-**4**.

Self-assembly of K_{12} structures on graphene of three additional molecules, i.e. **2-4** have been also simulated, and it was found that the structures based on molecules **2**, **3** and **4** ($K2_{12}$, $K3_{12}$ and $K4_{12}$) are stable over tens of nanoseconds of simulation time as in the case of $K1_{12}$.

5.2 Kagomé on Monolayer

To achieve a comprehensive understanding of the formation of bilayer structures, we simulated the self-assembly K_{12} structures of **1**, **2**, **3** and **4** on the pre-assemble monolayer architectures and underlying graphene slab. The super-cells of monolayer (Fig.S16) were obtained by multiplying the magnitude of the 6-molecule elementary rectangular unit cell vectors (i.e. the smallest rectangular unit cell) by 3 and 2, where the super-cell consists of 36 molecules.

CHARMM Keywords (formation of monolayer - example of **1**):

```
SET NN 1
SET ID 1
SET II 1
SET XX 1
SET YY 1
SET NMOL 36
SET NXCELL 3
SET NYCELL 2
LABEL LABELNN
….
COOR TRANS XDIR 15.62 SELECT SEGID MMFF END
CALC ANGLE @NN*60
COOR ROTA ZDIR 1 PHI @ANGLE SELECT SEGID MMFF END
IF @ID .eq. 3 THEN
COOR TRANS YDIR -27.69 SELE SEGID MMFF END
COOR TRANS XDIR 46.86 SELE SEGID MMFF END
ENDIF
IF @ID .eq. 2 THEN
COOR TRANS XDIR 31.24 SELE SEGID MMFF END
ENDIF
IF @ID .eq. 4 THEN
COOR TRANS XDIR 31.24 SELE SEGID MMFF END
ENDIF

CALC DX = @XX * 31.93
CALC DY = @YY * 55.3
COOR TRANS XDIR @DX SELE SEGID MMFF END
COOR TRANS YDIR @DY SELE SEGID MMFF END

CALC MM = 6 * @II
IF NN .ge. @MM THEN
  INCR II
```

```
  SET ID 0
  IF XX .lt. @NXCELL THEN
    INCR XX
  ELSE
     IF YY .lt. @NYCELL THEN
       INCR YY
       SET XX 1
     ENDIF
  ENDIF
ENDIF
INCR ID
INCR NN
IF NN .le. @NMOL GOTO LABELNN
```

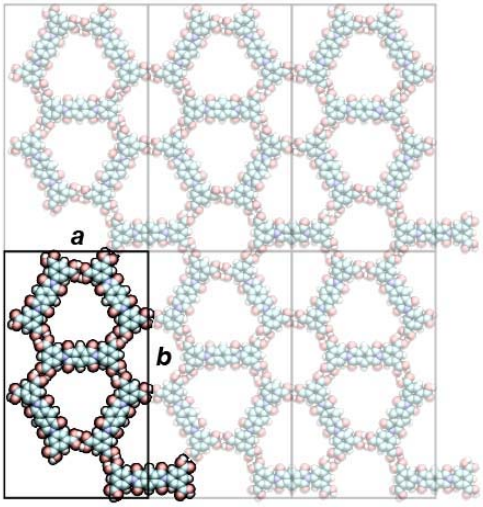

Figure S16. a) Rectangular super-cell used for the calculations of bilayer of **1**, based on multiples of elementary rectangular unit cell (marked in black). Unit cell parameters used for molecules **1**-**3**: *a* = 31.19 Å and *b* = 53.11 Å, whereas unit cell parameters for molecule **4**: *a* = 27.95 Å and *b* = 49.70 Å.

Manually pre-formed $\boldsymbol{K_{12}}$ structures have been initially placed 6Å above the monolayer slab (and 12 Å above the graphene slab), and positioned in the fully overlapped fashion in respect with the monolayer (marked in black on Fig.S17a), which was embedded in a orthorhombic box of lengths equal to 95.68 and 109.12 Å for the molecules **1-3** and equal to 84.76 and 98.24 Å for the molecule **4**, with periodic boundary conditions (PBCs) to simulate an infinite monolayer slab for all calculations. The interaction energy between the $\boldsymbol{K_{12}}$ and ***K*** monolayer structures (interlayer energy) was calculated by subtracting the energy upon displacement of the $\boldsymbol{K_{12}}$ 100Å away from the ***K*** monolayer.

Subsequently, 3 sets of 1620 independent energy calculations for **1-3** (3 sets of 1344 calculations each for **4**) were performed, where in case of **1-3** the surface of 16.2 nm^2 (marked in blue on Fig.S17b) have been mapped by analyzing interlayer energy evolution in 30×54

matrix (28×48 matrix for **4**), where the distance between equally distributed points was equal to 1.03Å. In such a way the fully overlapped $\boldsymbol{K_{12}}$ could be fully translated over the monolayer structure with respect to the initial structure: along X (marked in red on Fig.S17a) and Y (marked in blue on Fig.S17a); and twice along XY direction (marked in green on Fig.S17a).

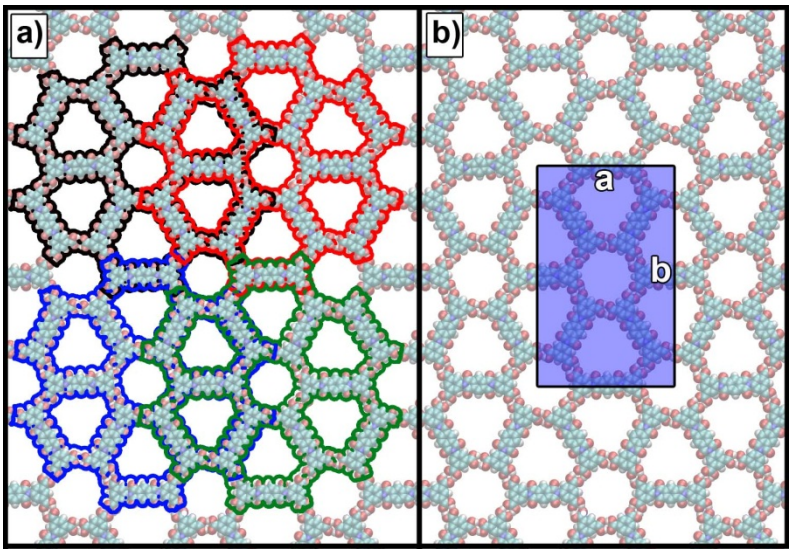

Figure S17. a) Schematic representation of initial fully overlapped (marked in black) and final fully translated structures of $\boldsymbol{K1_{12}}$ (marked in red, blue and green) on ***K*** monolayer, graphene slab has been removed for clarity; b) schematic visualization of area sampled by translating $\boldsymbol{K1_{12}}$ assembly, a = 30Å and b = 54Å.

Figure S18 shows the interlayer energy evolution of $\boldsymbol{K_{12}}$ structures, where interaction energy between $\boldsymbol{K_{12}}$ and ***K*** monolayer in the fully overlapped conformation were chosen as a reference points.

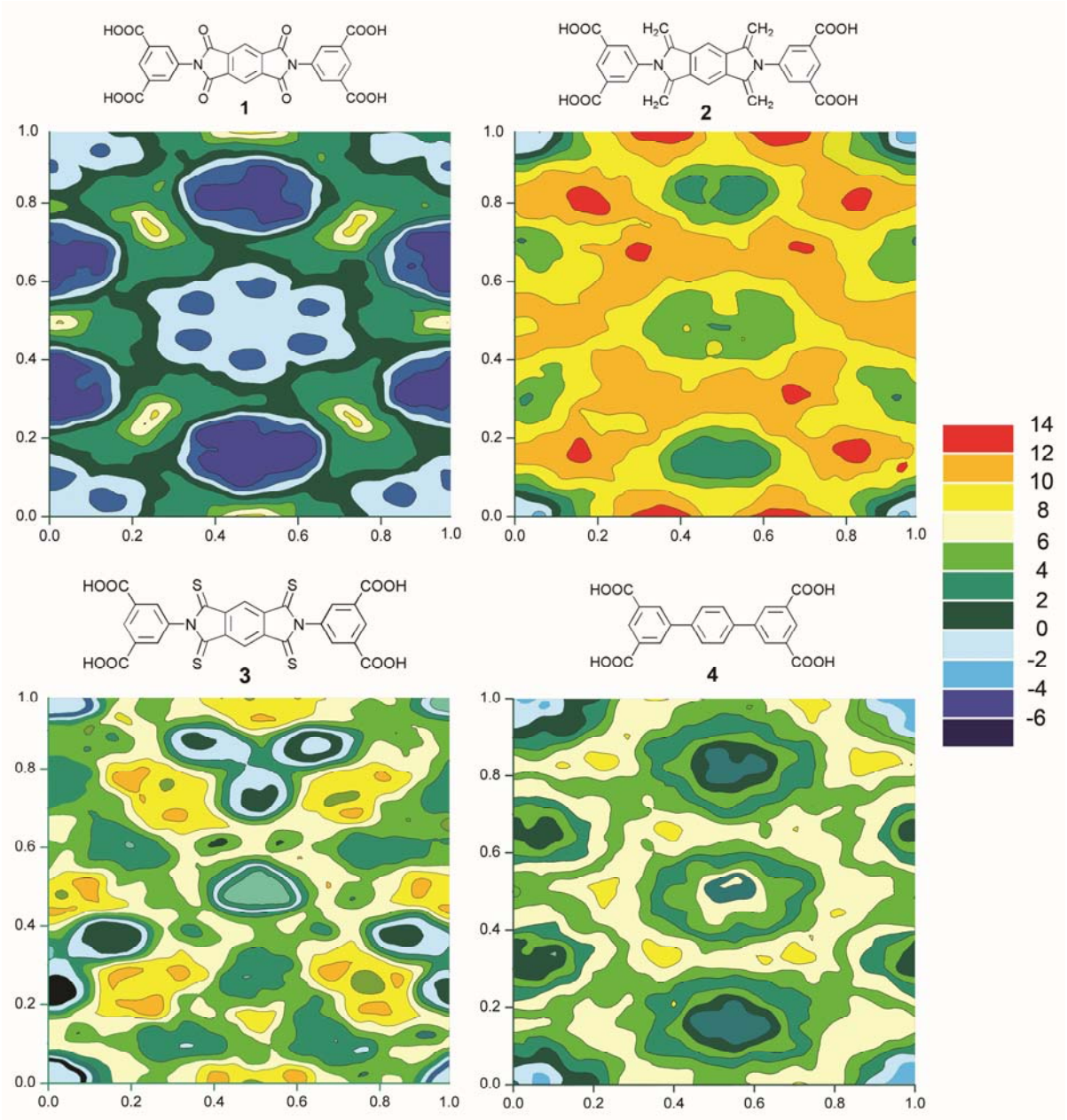

Figure S18. Interlayer energy evolution of single molecule **1** (a), **2** (b), **3** (c) and **4** (d) from K_{12} assemblies with underlying monolayer structures (energies given in kcal mol^{-1}).

5.2.1 *K1*$_{12}$ on *K1* monolayer

Figure S19a shows representative visualization of energetically favored conformation of ***K1*$_{12}$** structure on ***K1*** monolayer, determined by interlayer interaction energy evolution (Fig. S18a) where ***K1*$_{12}$** assembly has been shifted by 15Å in X and 8 Å in Y directions, with respect to the initial fully overlapped structure. Such a phenomenon can be explained by the repulsive interactions between oxygen atoms from carbonyl groups, which results in the shift of ***K1*$_{12}$** assembly.

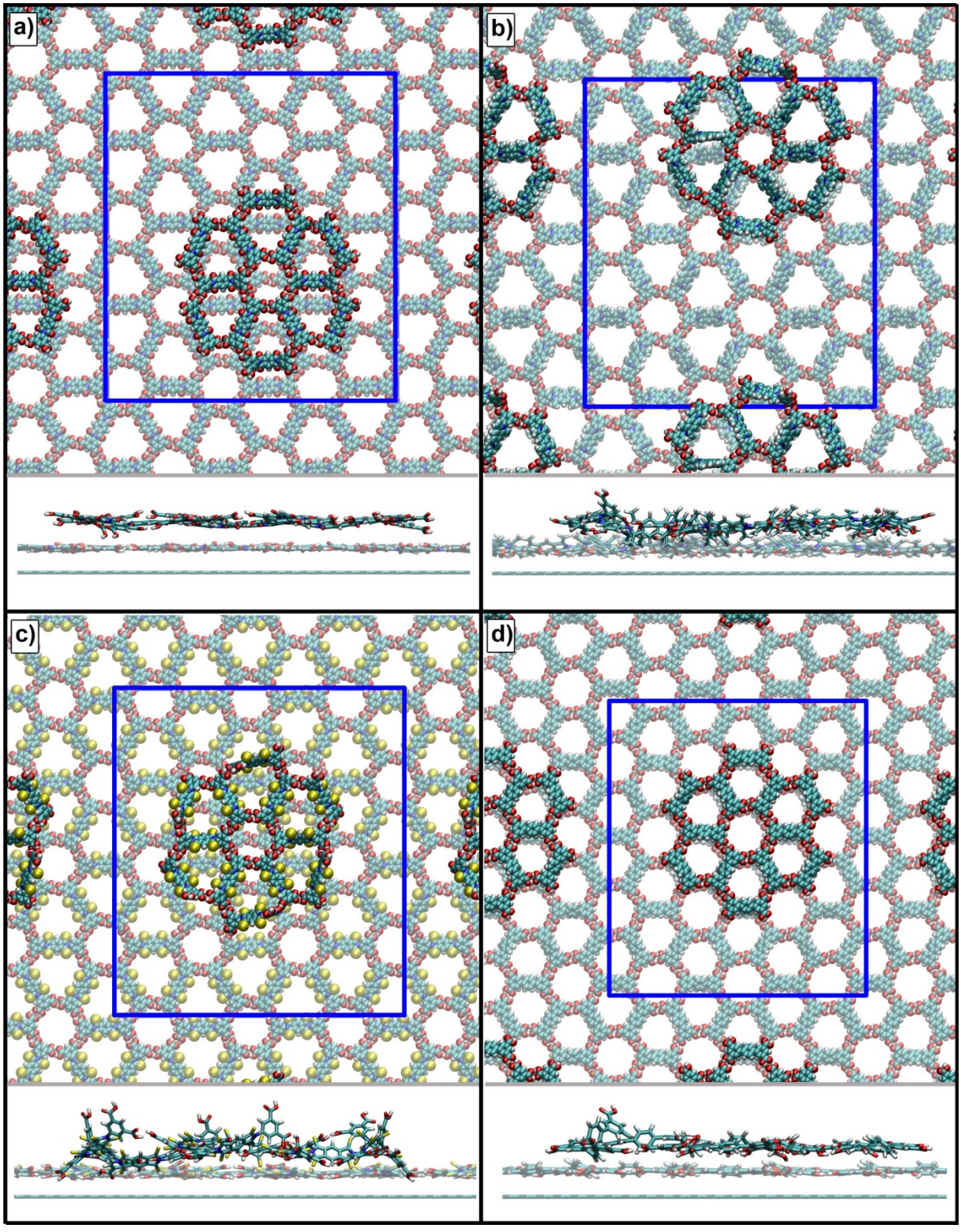

Figure S19. Representative visualization of the top and side views of energetically favored self-assembled structures of: $K1_{12}$ (a), $K2_{12}$ (b), $K3_{12}$ (c) and $K4_{12}$ (d) on the corresponding monolayer surfaces.) Rectangular super-cell used for the calculations has been marked in blue.

5.2.2 *K2*$_{12}$ on *K2* monolayer

Figure S19b shows the visualization of the energetically favored conformation of ***K2*$_{12}$** structure on ***K2*** monolayer (see Fig.S18b). Differently than in case of ***K1*$_{12}$+*K1***, where ***K1*$_{12}$** assembly has been shifted with respect to the initial fully overlapped structure, the highest interaction energy between ***K2*$_{12}$** and ***K2*** monolayer was observed when the two are fully overlapped, which indicates that the presence of oxygen atoms in the core of **1** is causing the shift of the ***K1*$_{12}$**.

5.2.3 *K3*$_{12}$ on *K3* monolayer

Figure S19c shows the visualization of the favored conformation of ***K3*$_{12}$** structure on ***K3*** monolayer (see Fig.S18c). Similar to the case of ***K1*$_{12}$+*K1***, ***K3*$_{12}$** has been shifted with respect to the initial fully overlapped structure. Such an observation suggests that whenever negatively charged atoms are introduced to the structure of molecular building block the shifted conformation is favored. Interestingly, differently than in case of ***K1*$_{12}$+*K1***, ***K3*$_{12}$** structure is not planar. Sulfur atoms which have lowest hydrogen-bonding affinity than oxygen atoms, cannot form H-bonds with hydrogen atoms from isophthalic group of molecule, therefore the molecules **3** are not planar in ***K3*$_{12}$** assembly. Remarkably, the molecule **3** can be planarized (not fully) once full monolayer is formed (see side view in Fig.S19c).

5.2.4 *K4*$_{12}$ on *K4* monolayer

Figure S19d shows representative visualization of energetically favored conformation of ***K4*$_{12}$** assembly on ***K4*** monolayer (see Fig.S18d). Similar to the case of ***K2*$_{12}$+*K2***, complete overlap of ***K4*$_{12}$** with underlying ***K4*** monolayer can be observed, which confirms that by removing partial atomic charges from the molecular building block fully eclipsed conformation is observed.

Figure S20 shows the evolution of dihedral angles of all investigated molecules, in the monolayer and ***K*$_{12}$** structures in the simulation time of 1ns. Among all investigated molecules only molecule **1** was found to be fully planar, due to the intramolecular H-bonding between oxygen atoms from carbonyl groups and hydrogen atoms from isophthalic moieties. By introducing methylene groups in the structure, non-planarity of molecule **2** was observed, which can be seen on Fig.S20. As mentioned above, sulfur atoms which have lowest hydrogen-bonding affinity than oxygen atoms, cannot form H-bonds with hydrogen atoms

from isophthalic group of molecule, therefore the molecules **3** are not planar in both ***K3*$_{12}$** assembly and monolayer structure. Interestingly, non-planarity of **4** is much higher in its ***K4*$_{12}$** assembly than in ***K4*** monolayer.

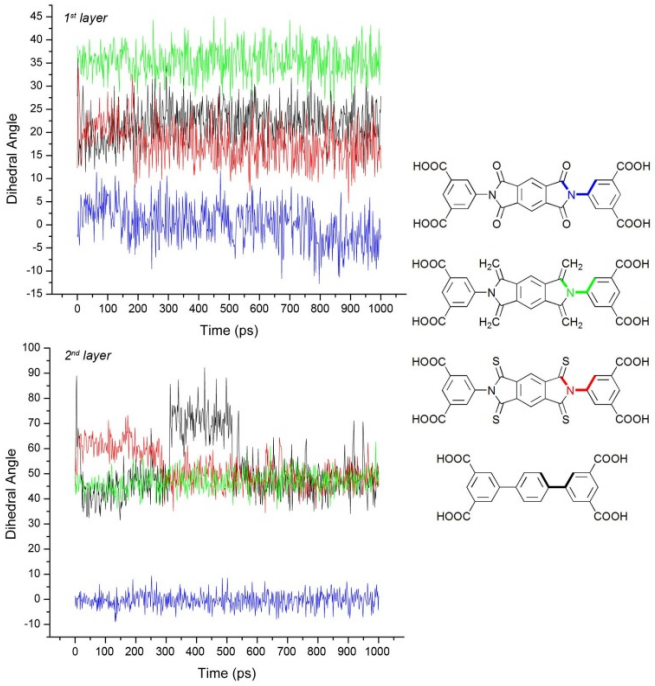

Figure S20. The evolution of dihedral angles of investigated molecules over 1ns of simulation time.

	Dihedral angle	
Molecule	1st layer	2nd layer
1	0.23 ± 4.22	-0.34 ± 2.96
2	35.44 ± 3.32	48.64 ± 3.91
3	17.74 ± 4.27	51.96 ± 7.15
4	21.98 ± 4.09	52.02 ± 12.14

Table S1. Average of dihedral angles of investigated molecules.

In order to rationalize the shifting of ***K1*$_{12}$** (as well as ***K3*$_{12}$**) with respect to the monolayer, the composition of the total energy for the four TCA derivatives, have been investigated. ***K12*** structures have been initially placed in their local minimum conformations in diferent energetical domains, as determined by intar-layer interaction studies. Subsequently, 10 independent energy calculations for **1-4** were performed, where eclipsed to shifted conformational transitions close to the minimum energy path (indicated with red lines Fig.S21) have been mapped by analyzing the evolution of total (E_{total}), electrostatic ($E_{elec.}$), van der Waals (E_{vdW}) and internal ($E_{int.}$) energies. Figure S21 shows that the 3D architectures

originates from a complex interplay between dispersive (van der Waals) and electrostatic interactions between 2D layers. Total interaction energy of the initial structures (starting points of the red lines), were chosen as a reference points. As stated in the Main Text, the presence of negatively charged groups in the core of the molecule (derivatives **1** and **3**) destabilizes the "eclipsed" interlayer arrangement for electrostatic repulsions and drives an overall displacement of the adlayer. By contrast, in the absence of partially charged substituents (derivatives **2** and **4**) the fully overlapped arrangement, which maximizes the contact area between layers, is preferred.

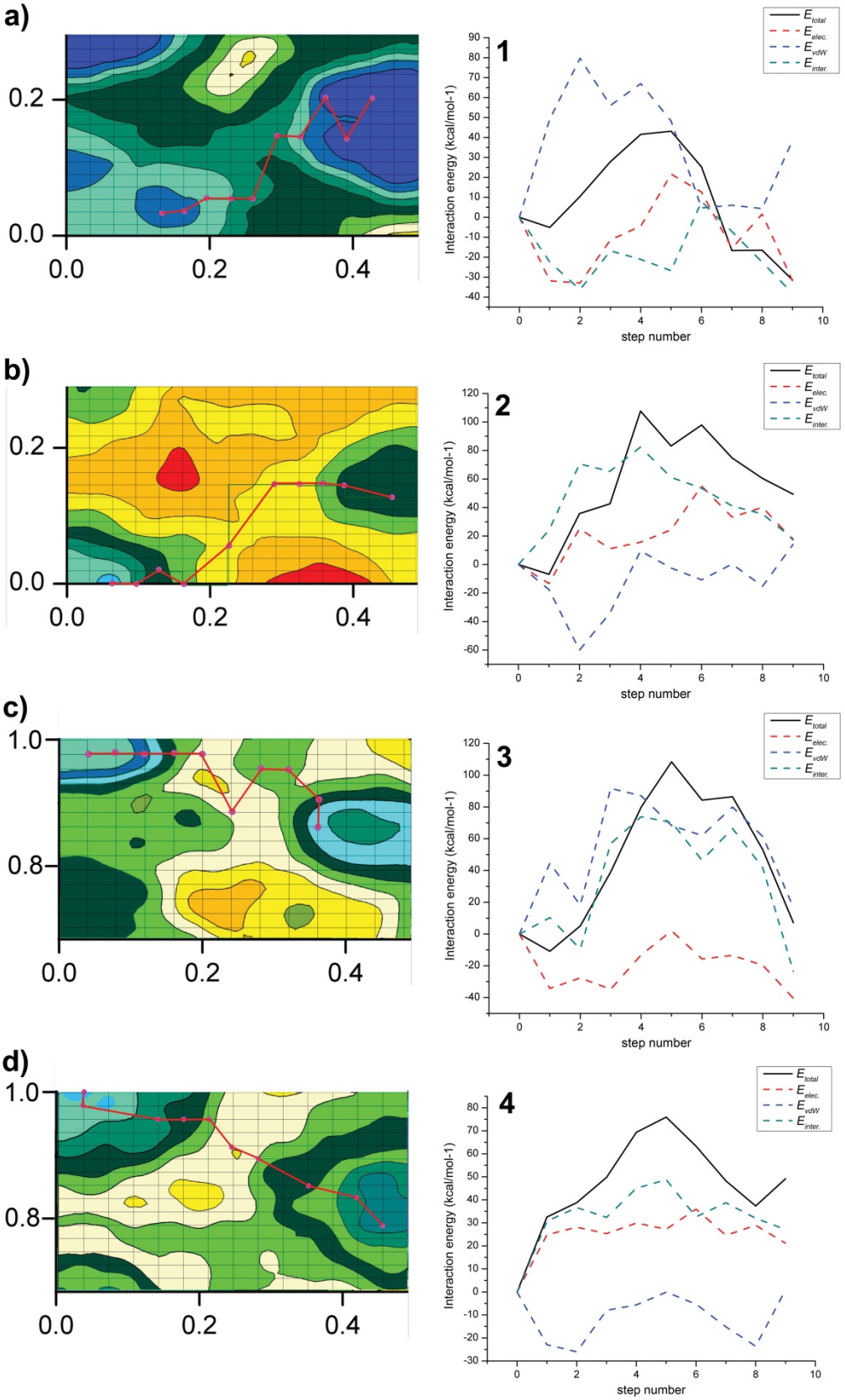

Figure S21. Evolution of total (E_{total}), electrostatic ($E_{elec.}$), van der Waals (E_{vdW}) and internal ($E_{int.}$) energies of investigated molecules over the pathway marked with red lines.

6. References

[1] a) H. Zhou, H. Dang, J. H. Yi, A. Nanci, A. Rochefort, J. D. Wuest, *J. Am. Chem. Soc.* **2007**, *129*, 13774-13775; b) M. Blunt, X. Lin, M. D. Gimenéz-López, M. Schröder, N. R. Champness, P. H. Beton, *Chem. Commun.* **2008**, 2304-2306; c) J. P. Garrahan, A. Stannard, M. O. Blunt, P. H. Beton, *Proc. Natl. Acad. Sci. U.S.A.* **2009**, *106*, 15209-15213; d) M. O. Blunt, J. C. Russell, M. D. Gimenéz-López, N. Taleb, X. L. Lin, M. Schröder, N. R. Champness, P. H. Beton, *Nat. Chem.* **2011**, *3*, 74-78.

[2] M. O. Blunt, J. C. Russell, M. D. Gimenéz-López, J. P. Garrahan, X. Lin, M. Schröder, N. R. Champness, P. H. Beton, *Science* **2008**, *322*, 1077-1081.

[3] M. Tarini, P. Cignoni, C. Montani, *IEEE T. Vis. Comput. Gr.* **2006**, *12*, 1237-1244.

[4] E. Runge, E. K. U. Gross, *Phys. Rev. Lett.* **1984**, *52*, 997-1000.

[5] a) A. D. Becke, *J. Chem. Phys.* **1993**, *98*, 5648–5652; b) C. T. Lee, W. T. Yang, R. G. Parr, *Phys. Rev. B* **1988**, *37*, 785–789.

[6] M. J. Frisch, G. W. Trucks, H. B. Schlegel, G. E. Scuseria, M. A. Robb, J. R. Cheeseman, J. Montgomery, J. A., T. Vreven, K. N. Kudin, J. C. Burant, J. M. Millam, S. S. Iyengar, J. Tomasi, V. Barone, B. Mennucci, M. Cossi, G. Scalmani, N. Rega, G. A. Petersson, H. Nakatsuji, M. Hada, M. Ehara, K. Toyota, R. Fukuda, J. Hasegawa, M. Ishida, T. Nakajima, Y. Honda, O. Kitao, H. Nakai, M. Klene, X. Li, J. E. Knox, H. P. Hratchian, J. B. Cross, V. Bakken, C. Adamo, J. Jaramillo, R. Gomperts, R. E. Stratmann, O. Yazyev, A. J. Austin, R. Cammi, C. Pomelli, J. W. Ochterski, P. Y. Ayala, K. Morokuma, G. A. Voth, P. Salvador, J. J. Dannenberg, V. G. Zakrzewski, S. Dapprich, A. D. Daniels, M. C. Strain, O. Farkas, D. K. Malick, A. D. Rabuck, K. Raghavachari, J. B. Foresman, J. V. Ortiz, Q. Cui, A. G. Baboul, S. Clifford, J. Cioslowski, B. B. Stefanov, G. Liu, A. Liashenko, P. Piskorz, I. Komaromi, R. L. Martin, D. J. Fox, T. Keith, M. A. Al-Laham, C. Y. Peng, A. Nanayakkara, M. Challacombe, P. M. W. Gill, B. Johnson, W. Chen, M. W. Wong, C. Gonzalez, J. A. Pople, **2004**, *Gaussian 03, Revision C.02, Gaussian, Inc., Wallingford CT*.

[7] http://www-curri.u-strasbg.fr/.

[8] D. Lee, W. Anderson, CRC Press, FL, **2007**.

[9] K. W. Hipps, Springer Verlag: New York, **2006**.

[10] B. R. Brooks, R. E. Bruccoleri, B. D. Olafson, D. J. States, S. Swaminathan, M. Karplus, *J. Comput. Chem.* **1983**, *4*, 187-217.

[11] T. A. Halgren, *J. Comput. Chem.* **1996**, *17*, 490-519.

[12] W. Humphrey, A. Dalke, K. Schulten, *J. Molec. Graphics* **1996**, *14*, 33-38.

[13] J. Björk, F. Hanke, C. A. Palma, P. Samorì, M. Cecchini, M. Persson, *J. Phys. Chem. Lett.* **2010**, *1*, 3407-3412.

[14] J. P. Ryckaert, G. Ciccotti, H. J. C. Berendsen, *J. Comput. Phys.* **1977**, *23*, 327-341.